Int. J. Electrochem. Sci., 14 **(2019)** 44 – 58, doi: 10.20964/2019.01.14

International Journal of
ELECTROCHEMICAL
SCIENCE
www.electrochemsci.org

Influence of aging paths on the thermal runaway features of lithium-ion batteries in accelerating rate calorimetry tests

Xuning Feng[1], *Dongsheng Ren*[2], *Shunchao Zhang*[2], *Xiangming He*[1,*], *Li Wang*[1], *Minggao Ouyang*[2,**]

[1] Institute of Nuclear and New Energy Technology, Tsinghua University, Beijing 100084, P R China;
[2] State Key Laboratory of Automotive Safety and Energy, Tsinghua University, Beijing 100084, P R China
[*]E-mail: hexm@mail.tsinghua.edu.cn; ouymg@mail.tsinghua.edu.cn

Received: 2 September 2018 / *Accepted:* 12 October 2018 / *Published:* 30 November 2018

Aging is inevitable during the use of lithium-ion batteries. However, the influence of aging paths on the safety of the lithium-ion batteries remains unclear, leaving uncertainties about safe operation throughout their full life cycle. This paper studies the influence of aging paths on the thermal runaway features in lithium-ion batteries using ARC. Characteristic temperatures are defined to quantify the thermal stability of lithium-ion batteries. Two kinds of aging tests are designed, high-temperature storage and low-temperature cycling. The effects of aging on the change in the characteristic temperatures have been investigated, providing a quantified analysis of the evolution of battery safety performance during aging. The thermal stability of the cells after low-temperature cycling is worse than that of the fresh cells and less than that of the cells that are treated by high-temperature exposure. Although the capacity retention rates of the cells aged by high-temperature exposure and low-temperature cycling can be similar, their thermal stabilities are quite different. The consumption of active lithium at the anode surface to generate a new SEI layer will result in a better thermal stability in the cells that are treated by high-temperature exposure. However, if there is lithium deposition on the surface of the anode, the thermal stability of the lithium-ion battery will become worse. The quantitative discussions and conclusions of this paper can provide guidance on evaluating the safety throughout the full life cycle.

Keywords: lithium-ion battery; energy storage; battery safety; thermal runaway; aging

1. INTRODUCTION

The world is marching into a cleaner era with greater utilization of renewable energies. The fluctuations in the power output of renewable energy sources need to be tuned by energy storage systems, for which battery storage is one of the most promising choices. Lithium-ion batteries, with high energy density and long life cycles, have been regarded as one of the best choices for today's electrochemical

energy storage systems [1-3]. The development of lithium-ion batteries has advanced the commercialization of electric vehicles in recent years [4-6]. The limited space on board requires lithium-ion batteries to have high energy density if we want the electric vehicles to have comparable operational ranges to those of engine-powered vehicles. However, high energy density brings safety problems and has attracted increasing attentions in adjacent research fields [7-12].

Thermal runaway (TR) is the core phenomenon during battery failure, it can lead to severe hazards such as vents, fire or explosion that threaten public safety [13]. Battery TR releases a large amount of heat in a very short time and is caused by uncontrolled chain reactions of the cell components [14]. Calorimetry, e.g., accelerating rate calorimetry (ARC), can be utilized to characterize heat generation during TR. ARC can provide an adiabatic test environment and is thereby being widely adopted for TR characterizations [15-18].

Aging is inevitable during battery use [19-21], with capacity depletion [22-24] and resistance growth [25-27]. However, how aging paths influence battery safety remains unclear. If the characteristics of TR deteriorate as aging continues, there will be potential safety issues for the aged cells that are in service. As most of the test standards/regulations only require abuse tests for fresh cells, the safety of lithium-ion batteries may be questionable after days of usage. Fleischhammer et al. [28] investigated the safety of unaged and aged high-power 18650 lithium-ion cells using ARC. The aging tests were conducted by high-rate and low-temperature cycling. They found that there are strong correlations between aging history and safety, whereas lithium plating may lead to an increase in heat generation during TR. Lammer et al. [29] compared gas release during thermal failure in un-aged and aged cells. The cell aging tests were conducted by cycling and high-temperature storage. They found that the total gas and heat emissions from cycled cells were larger than those from cells stored at high temperature. Zhang et al. [30] investigated the effect of calendar aging on the thermal safety of 4.6 Ah pouch cells. They thought that the thermal stability would improve after aging. Characteristic temperatures were defined and used as criteria to compare the thermal stability of cells at different levels of aging in Zhang's work, providing guidance for further quantitative analysis of the aging effects on battery safety performance.

This paper aims to study influence of the aging paths on the TR features of lithium-ion batteries using ARC. First, three characteristic temperatures are defined to quantify the thermal stability of lithium-ion batteries. The effects of aging on changes at those three characteristic temperatures are investigated, providing a quantified analysis of the evolution of battery safety during aging. Two kinds of aging paths are selected to represent high-temperature storage and low temperature cycling. The underlying relationships between aging mechanisms and the TR features are discussed. The work provides guidance on the evaluation of safety performances during battery aging.

2. EXPERIMENTAL SETUP

2.1 The battery cell

A 20Ah commercial pouch lithium-ion battery is used in this study. The battery cell has $Li_yNi_{1/3}Co_{1/3}Mn_{1/3}O_2$+ $Li_yMn_2O_4$ composite cathode [31]. The mass ratio between $Li_yNi_{1/3}Co_{1/3}Mn_{1/3}O_2$

and $Li_yMn_2O_4$ is 1:1. To measure the internal temperature of the cell during TR, two pouch cells are connected in parallel to form a "Large Cell" [32], as shown in Fig. 1. Therefore, in further cycling tests, we use the "Large Cell" with a capacity of 40 Ah as the basic unit.

2.2 The ARC tests

An accelerating rate calorimeter (ARC) manufactured by Thermal Hazard Technology® (THT) is utilized to conduct TR tests of the "Large Cell" samples. Although the "Large Cell" has a relatively large size, the ARC with an extended-volume chamber can hold large format samples, as shown in Fig. 1. The thermocouple (TC_1) is inserted between the two cells to measure the internal temperature of the "Large Cell". The sensor of the ARC is pasted on the surface of the sample, marked as TC_2 in Fig. 1, to guarantee an adiabatic test environment. The TR tests are conducted under the heat-wait-seek-exotherm mode. The ARC forms an adiabatic boundary condition around the cell during the exotherm mode, ensuring accurate measurement of the heat generation during TR. The ARC tests are conducted for cells before and after aging tests, and the TR features are compared.

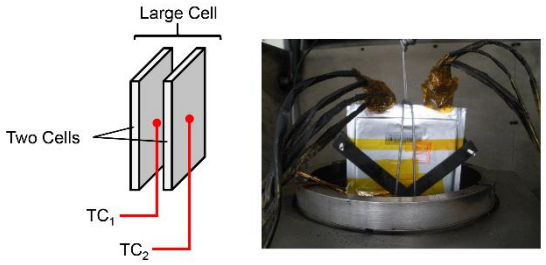

Figure 1. Test settings in an ARC chamber with extended-volume.

2.3 The characteristic temperatures during thermal runaway

Fig. 2(a) displays the three characteristic temperatures {T_1, T_2, and T_3} for battery TR. T_1 is the onset temperature of obvious self-heat generation by the battery sample. In an ARC test, T_1 occurs when the ARC detects an obvious temperature rise in the battery sample, usually judged by a preset threshold, e.g., 0.01℃·min^{-1}. T_1 reflects the thermal stability of the lithium-ion battery. A lower T_1 indicates that the cell is less thermally stable. T_2 is the triggering temperature of TR. The instantaneous heat release starts at T_2. A lower T_2 indicates that the cell is more prone to TR. T_3 is the maximum temperature that the battery can reach during a TR. The difference $\Delta T=T_3-T_2$ directly reflects the total heat released during a TR (ΔH_{TR}), as shown in Eqn. (1):

$$\Delta H_{TR} = C_p \cdot (T_3 - T_2) \quad (1)$$

where C_p is the specific heat capacity, and the unit of ΔH_{TR} is J·kg^{-1}. ΔH_{TR} reflects the intensive heat generation during TR. {T_1, T_2, and T_3} and the correlated parameters may change after aging. The changes in the {T_1, T_2, and T_3} are further used to quantitatively evaluate the aging effects on the battery safety performances.

2.4 The aging tests

Reference performance tests (RPT) are conducted to calibrate the capacity of the cell at different aging moments. The RPT test is conducted at 25℃ using a current of 13.33 A, which is 1/3C of the sample. The discharge curve is used for further analysis of the aging mechanisms. The capacity retention rate (*CRR*) is defined to judge the degree of capacity degradation as in Eqn. (2):

$$CRR = \frac{Q}{Q_{\text{init}}} \times 100\% \tag{2}$$

where Q is the discharge capacity and Q_{init} is the initial capacity of the fresh cell. *CRR* is further used to quantify the degree of aging.

Aging tests with two different paths are designed in this study, as shown in Fig. 2. One aging test is the high-temperature exposure test using ARC. This test is called the ARC test with early termination [33]. As shown in Fig. 2(a), the sample is heated by ARC, using the same procedure for conducting a full TR test. However, the ARC test will be terminated at a specific temperature T_{cool}, marked in blue in Fig. 2(a). Once the temperature of the sample reaches T_{cool}, the heat process is switched off, and the sample is cooled down to ambient temperature. After high-temperature exposure to T_{cool}, there is obvious capacity degradation of the cell, as reported in Ref. [33]. Since the capacity degradation by high-temperature exposure is similar to that by cycling at high-temperature, we use the test profile in Fig. 2(a) to save time. T_{cool}={80℃, 90℃, 100℃, 110℃} is set in the experiments. After one high-temperature exposure, the cell is further cycled by the RPT test until the *CRR* is stable.

The other aging test is the low-temperature cycling test, as shown in Fig. 2(b). The cell is cycled by a CC-CV charging and CC discharging profile at -10 ℃. The current for the CC segment is chosen as 4 A, which is 1/10 C of the sample. Lithium deposition occurs fast at such a low temperatures by CC-CV charging; therefore fast capacity degradation can be achieved. After several cycles at low temperature, the *CRR* is checked using the RPT profile.

All the samples are tested using the ARC to characterize the TR features after aging; therefore, the effect of aging paths on the battery safety performances can be evaluated.

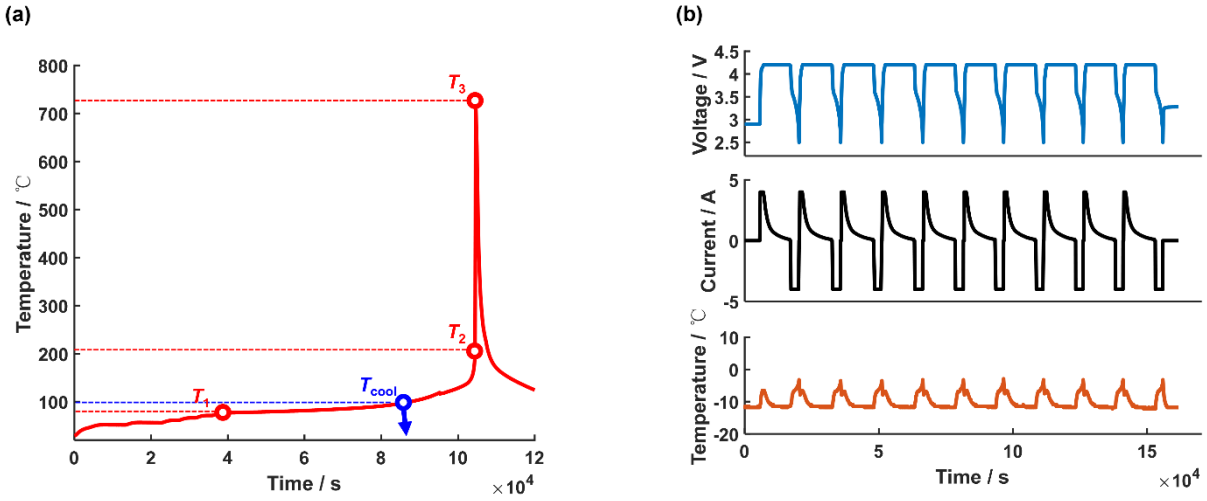

Figure 2. The different aging paths set in the tests. (a) High-temperature exposure by ARC heating. (b) Low temperature (-10℃) cycling profile.

3. THEORETICAL DEVELOPMENT

The mechanism of battery aging is quantitatively investigated using a mechanistic and diagnostic (M&D) model, proposed by Christensen and Newman [34]. The M&D model comprises Eqn. (3) to Eqn. (5) [35,36]. The voltage output of the model can be calculated by Eqn. (3):

$$V_{\mathrm{mdl}} = V_{\mathrm{ca}}(y) - V_{\mathrm{an}}(x) - I \cdot R \tag{3}$$

where V_{mdl} is the voltage predicted by the model, V_{ca} is the cathode voltage, V_{an} is the anode voltage. I is the current, R is the overall resistance and y and x are the stoichiometric coefficients of the cathode and anode, respectively. The relationships of $V_{\mathrm{ca}}(y)$ and $V_{\mathrm{an}}(x)$ are acquired by a half-cell test, as shown in Fig. 3. y and x are updated by Eqn. (4) and (5), respectively.

$$y = y_0 + \int_0^t \frac{I}{Q_{\mathrm{ca}}} \mathrm{d}\tau \tag{4}$$

$$x = x_0 - \int_0^t \frac{I}{Q_{\mathrm{an}}} \mathrm{d}\tau \tag{5}$$

where y_0 and x_0 are the initial values of y and x, respectively, t is the time and Q_{ca} and Q_{an} are the capacities of the cathode and anode, respectively.

The M&D model can fit the discharge curve in the RPT test by setting proper parameters $\{Q_{\mathrm{ca}}, Q_{\mathrm{an}}, y_0, x_0, R\}$, as shown in Fig. 3. Conversely, we can identify the set of $\{Q_{\mathrm{ca}}, Q_{\mathrm{an}}, y_0, x_0, R\}$ through the discharge data recorded in the RPT test. From the RPT test, we can acquire a set of $\{t, V_{\mathrm{exp}}, I\}$, where V_{exp} is the measured discharge voltage, and I = 1/3 C is the current. An optimization algorithm, e.g., the genetic algorithm, is used to identify the optimal set of parameters $\{Q_{\mathrm{ca}}, Q_{\mathrm{an}}, y_0, x_0, R\}$ for the model to fit the experimental data $\{t, V_{\mathrm{exp}}, I\}$, as Han et al. did in [37]. The fitness function used for the optimization algorithm is RMSE, the root mean square error between the V_{mdl} and V_{exp}, as defined in Eqn. (6). The optimization algorithm uses RMSE as a quantified criterion to iterate and to find an optimal solution. Note that Eqn. (6) is a discrete expression because the sampling interval during discharge is 1 s. Γ is the total time taken in the discharge process.

$$RMSE = \sqrt{\frac{1}{\Gamma}\sum_{t=1}^{\Gamma}\left(V_{\mathrm{mdl}}(t) - V_{\mathrm{exp}}(t)\right)^2} \tag{6}$$

The identified $\{Q_{\mathrm{ca}}, Q_{\mathrm{an}}, y_0, x_0, R\}$ directly links to the aging mechanisms of the lithium-ion battery. The loss of active material (LAM) can be reflected by the decrease in Q_{ca} or Q_{an}, the loss of lithium inventory (LLI) can be reflected by y_0 and x_0, and the ohmic resistance increase (ORI) can be reflected by the increase in R.

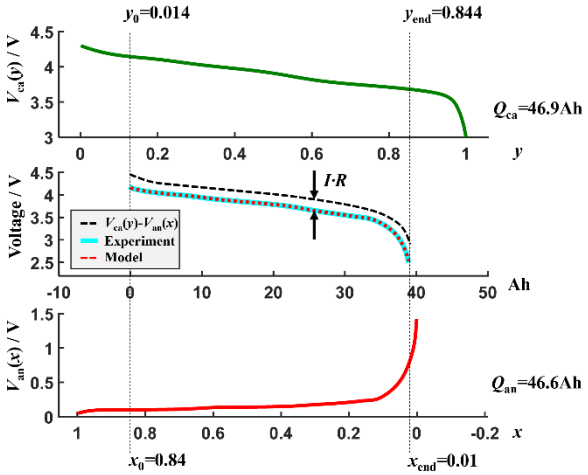

Figure 3. The mechanistic and diagnostic model for capacity degradation analysis.

4. RESULTS AND DISCUSSION

4.1 Aging mechanism after high-temperature exposure

This section discusses the aging mechanism after high-temperature exposure. Fig. 4(a) shows that after high-temperature exposure to T_{cool}= 80℃, 90℃, 100℃, and 110℃, the CRRs are 95.0%, 91.8%, 73.2%, and 50.3%. Fig. 4(b) illustrates the discharge voltages for the fresh cells and for the cells after high-temperature exposure. Obvious aging can be observed; therefore, further investigation of the changes in TR features will be meaningful.

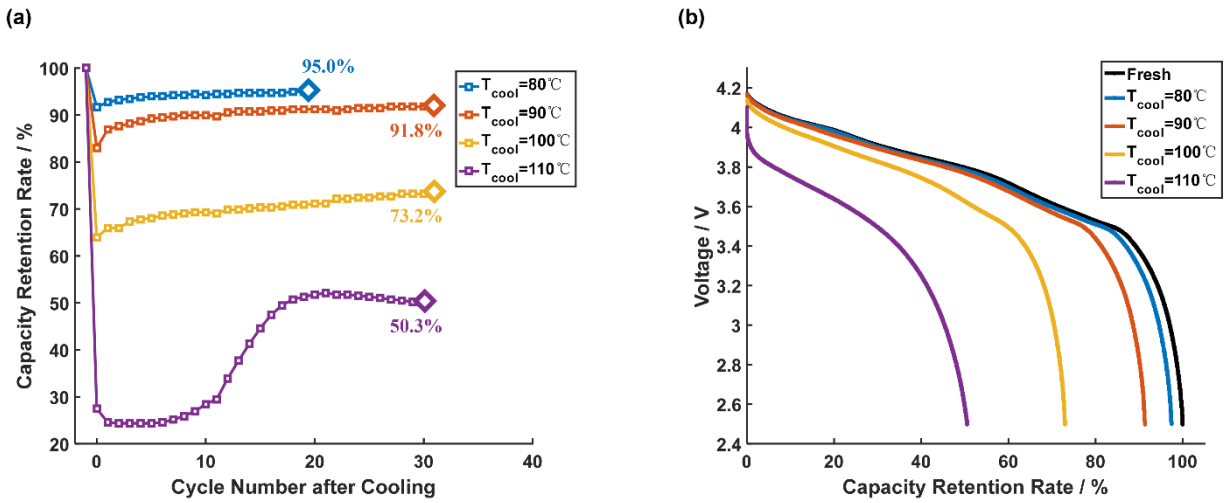

Figure 4. The aging features after high-temperature exposure. (a) The capacity retention rate after cooling from high-temperature. (b) The discharge voltage after high-temperature exposure.

Fig. 5(a) shows the calculated incremental capacity (IC) and dQ/dV for the cell after high-temperature exposure. LLI can be inferred for T_{cool}≥90℃ because the right most peak is vanishing [37].

LAM is also severe, because the IC for the cell exposed to T_{cool}=110℃ shrinks to a single peak. Quantified analysis of the degradation mechanisms can be acquired by the method introduced in Sec. 3. {Q_{ca}, Q_{an}, y_0, x_0, R} can be identified from the discharge data in the RPT tests, for cells exposed to different T_{cool}. Fig. 5(b) shows that once T_{cool}≥90℃, there will be an obvious decrease in Q_{ca} and Q_{an}, indicating large amount of LAM. LLI can be inferred from the decrease in x_0, although y_0 does not change monotonically. The ORI becomes obvious for the cells with T_{cool}=110℃, due to cell swell caused by solvent evaporation and the gas generation by SEI decomposition. We have to admit that the mechanism of capacity degradation under high temperature exposure in this study deviates a bit from that in the real applications [38]. Although the aging is quite accelerated, the extreme temperature set in the test may lead to cell leakage, which brought unexpected LAM and ORI [33]. Nevertheless, the data collected here is suitable for establishing an electrochemical-thermal coupled battery TR model [39], which will be reported in our future work.

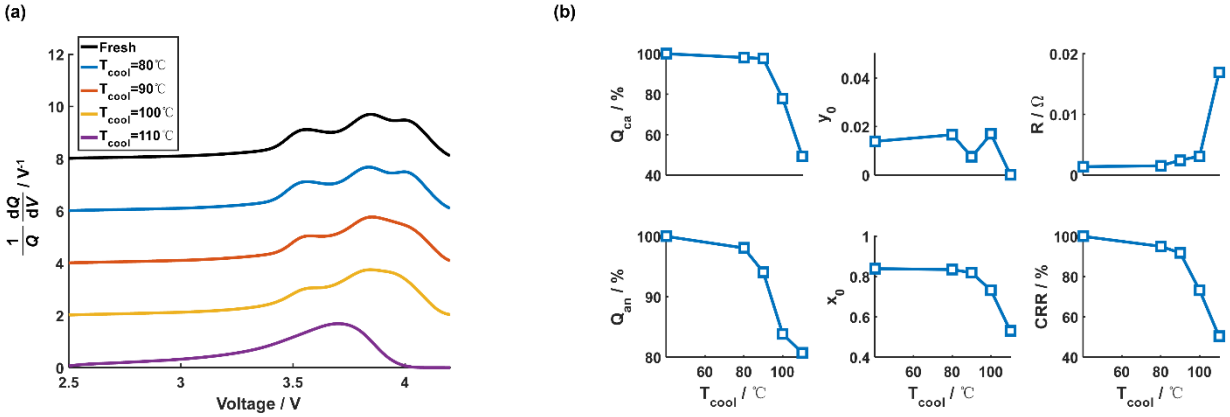

Figure 5. Interpretation of the aging mechanisms of the lithium-ion cells after high-temperature exposure. (a) The IC curves. (b) The identified parameters that can reflect the LLI, LAM and ORI in the M&D model.

In order to evaluate the LLI within the cell, the total lithium inventory Σ(Li/Li$^+$) is defined by Eqn. (7):

$$\sum(\mathrm{Li}/\mathrm{Li}^+) = \mathrm{Li}_{ca} + \mathrm{Li}_{an} + \mathrm{Li}_{electrolyte} \approx Q_{ca} \cdot y_0 + Q_{an} \cdot x_0 \quad (7)$$

where Σ(Li/Li$^+$) is defined as the sum of the product of Q_{ca}·y_0 and Q_{an}·x_0. Fig. 6(a) shows the Σ(Li/Li$^+$) for different T_{cool}, calculated from the data in Fig. 5(b) using Eqn. (7). Σ(Li/Li$^+$) has a good linear relationship with CRR, as shown in Fig. 6(b), therefore the major capacity loss can be explained by the loss in Σ(Li/Li$^+$) for the cells under high-temperature exposure.

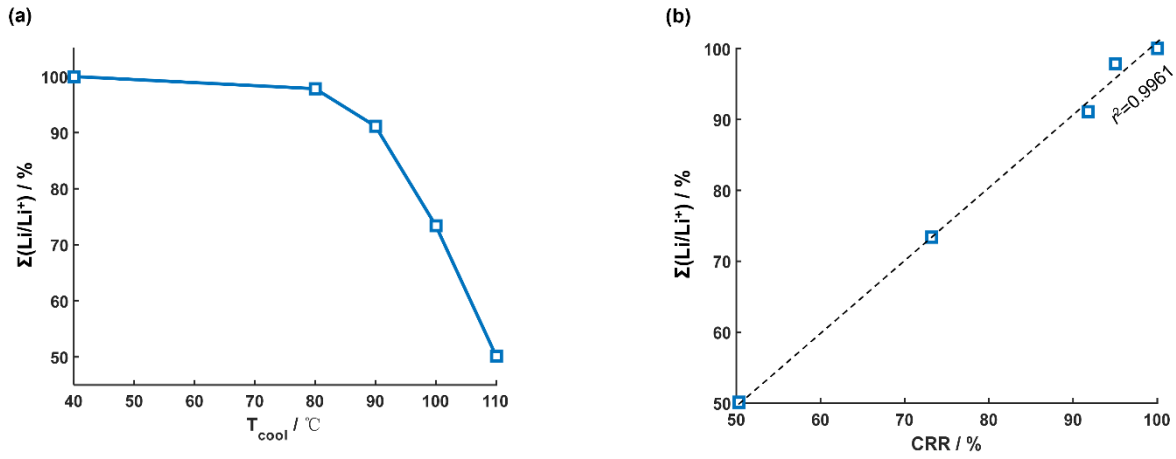

Figure 6. The loss of lithium inventory caused by high-temperature exposure. (a) $\Sigma(Li/Li^+)$ vs. T_{cool}. (b) the linear correlations between $\Sigma(Li/Li^+)$ and CRR.

4.2 Aging mechanism after low-temperature exposure

This section discusses the aging mechanism after low-temperature cycling. Fig. 7(a) shows that after low-temperature cycling for 15, 30, 40, and 50 cycles, the CRR are 95.4%, 90.4%, 86.3%, and 78.4%, respectively. Fig. 7(b) shows the discharge voltage for the fresh cells and for the cells after low-temperature cycling. The capacity degradation stops at approximately 80%, which is regarded as the end of life for lithium-ion batteries.

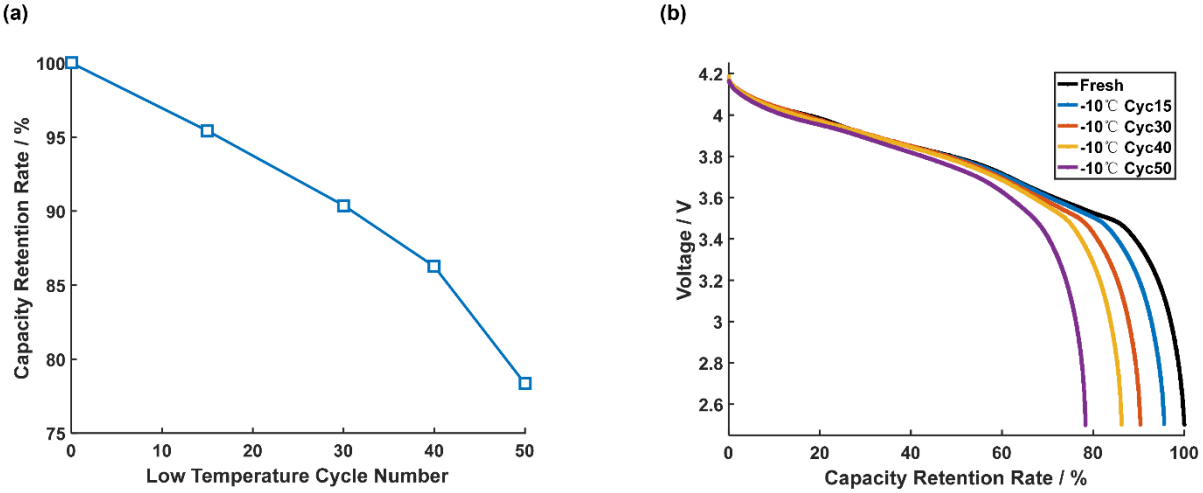

Figure 7. The aging features after low temperature cycling. (a) The capacity retention rate after cycling at low temperature. (b) The discharge voltage after cycling at low temperature.

Fig. 8(a) shows the calculated IC of the cells that are cycled at low temperature. The vanishing of the right-most peak indicates the LLI at the anode, whereas the shrinkage of the distance between the peaks indicates that LAM occurs continuously during cycling. Fig. 8(b) displays the quantified analysis of the changes in $\{Q_{ca}, Q_{an}, y_0, x_0, R\}$ during low-temperature aging. The decrease in x_0 indicates that lithium deposition occurs continuously during low-temperature cycling. Q_{ca} and Q_{an} first increase and

then decrease during cycling. The resistance is slightly lower after low-temperature cycling, indicating that the deposited lithium may form better tunnels for Li to travel from the electrolyte into the anode.

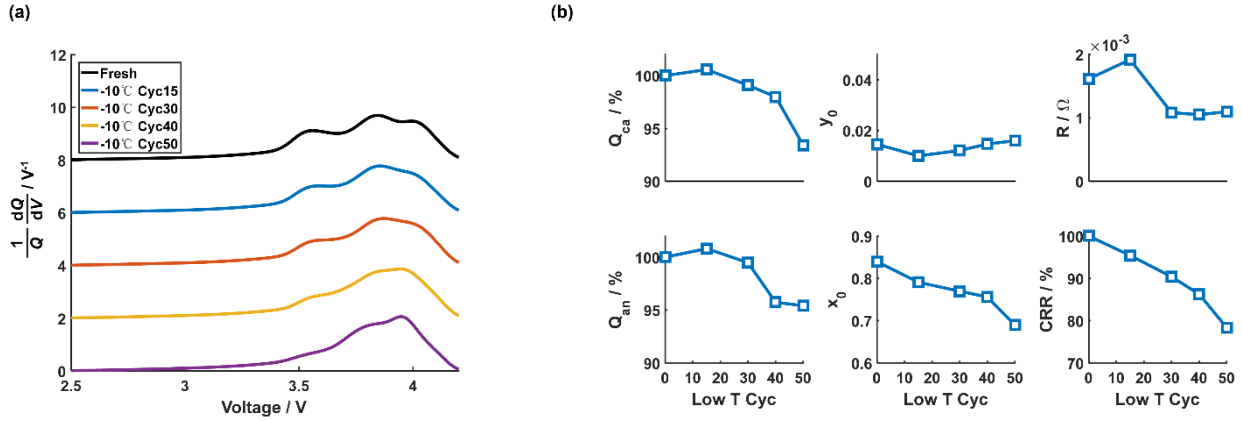

Figure 8. Interpretation of the aging mechanisms of the lithium-ion cells after low-temperature cycling. (a) The IC curves. (b) The identified parameters that can reflect the LLI, LAM and ORI in the M&D model.

Fig. 9(a) shows the $\Sigma(Li/Li^+)$ for cells cycled at low-temperature calculated from the data in Fig. 8(b) using Eqn. (7). The $\Sigma(Li/Li^+)$ for low-temperature cycling also has a good linear relationship with CRR, as shown in Fig. 9(b); therefore, the major capacity loss can also be explained by the loss in $\Sigma(Li/Li^+)$ for the cells under low-temperature cycling. However, note that the LLI for low-temperature cycling is different from that for high temperature exposure. The LLI at low-temperature is mainly caused by the lithium deposition on the anode surface [40], rather than the reactions with the electrolyte to form new SEI at high temperature [33]. This difference lead to difference in the heat generation rate reported by ARC test, which will be discussed in the following sections.

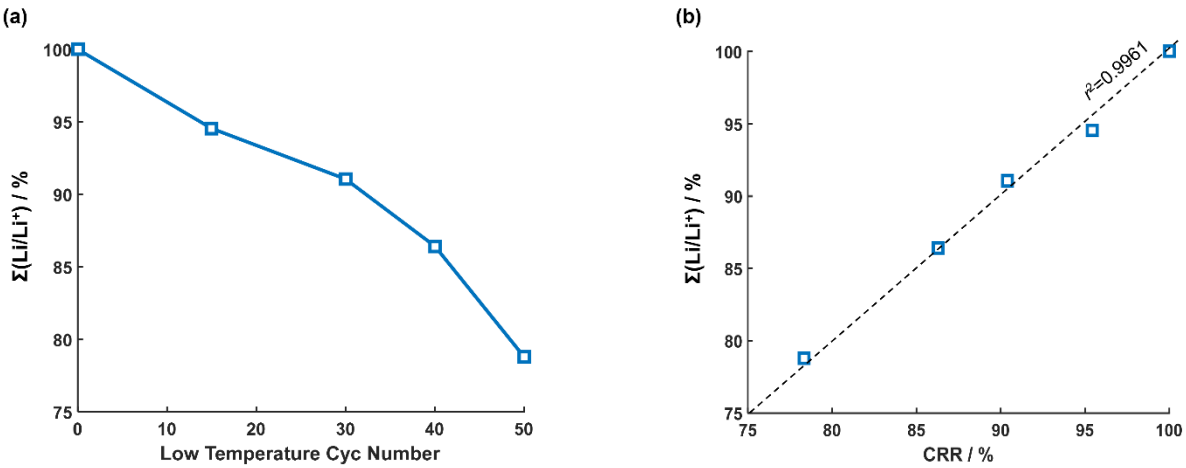

Figure 9. The loss of lithium inventory caused by low-temperature cycling. (a) $\Sigma(Li/Li^+)$ vs. cycle numbers. (b) the linear correlations between $\Sigma(Li/Li^+)$ and CRR.

4.3 The influence of aging by high-temperature exposure on the thermal runaway features

This section discusses the influence of aging by high-temperature exposure on the TR features of lithium-ion batteries. Fig. 10 compares the dT/dt vs. T curves for cells exposed to different T_{cool}. Fig. 10(a) presents an overall view of the rate of temperature increase. The dT/dt at T>200℃ for higher T_{cool} is less than that for lower T_{cool}, indicating that the overall heat generation is reduced after high-temperature storage. Fig. 10(b) gives a magnified view of dT/dt at T<200℃, where dT/dt decreases at 120℃<T<200℃ as T_{cool} increases, reconfirming the argument that the thermal stability is improved after high-temperature exposure. T_1 is increasing for T_{cool}≤100℃, however, for T_{cool}=110℃, T_1 drops to 60.9℃, which deviates from the consistent behavior of cells after high-temperature exposure. The interpretation of this phenomenon will be discussed in Sec. 4.5.

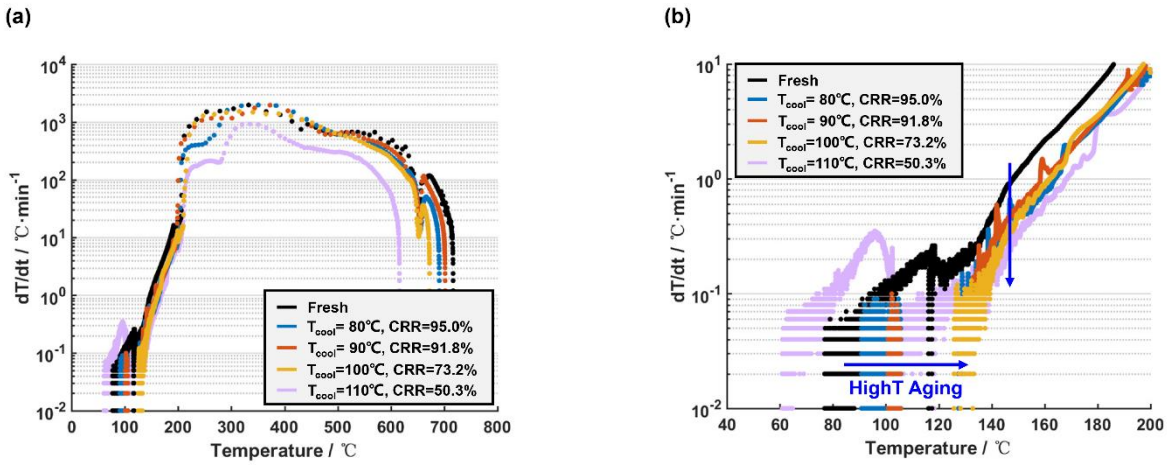

Figure 10. The temperatrue rise rate for fresh cell and aged cells after high-temperature exposure. (a) The overall curve for dT/dt vs. T. (b) The magnified figure of (a) for temperture lower than 200℃.

Fig. 11 collects the key features of TR for cells aged by different T_{cool}. Fig. 11(a) shows that as T_{cool} increases, T_3 drops, T_2 rises, and T_1 rises then drops. Fig. 11(b) compares the values of T_3-T_2 and the specific energy that is released during TR (ΔH_{TR}), as defined in Eqn. (1), for different T_{cool}. An obvious decreasing trend can be observed, and the rate of decrease in ΔH_{TR} vs. CRR is approximately 2.35×10^3 J·kg^{-1}·%$^{-1}$, which means that 1% decrease in the CRR will bring a 2.35×10^3 J·kg^{-1} decrease in ΔH_{TR}. The results here can be inferred to that a cell aged by high temperature cycling will be safer than itself at fresh condition, similar results can be seen in [28].

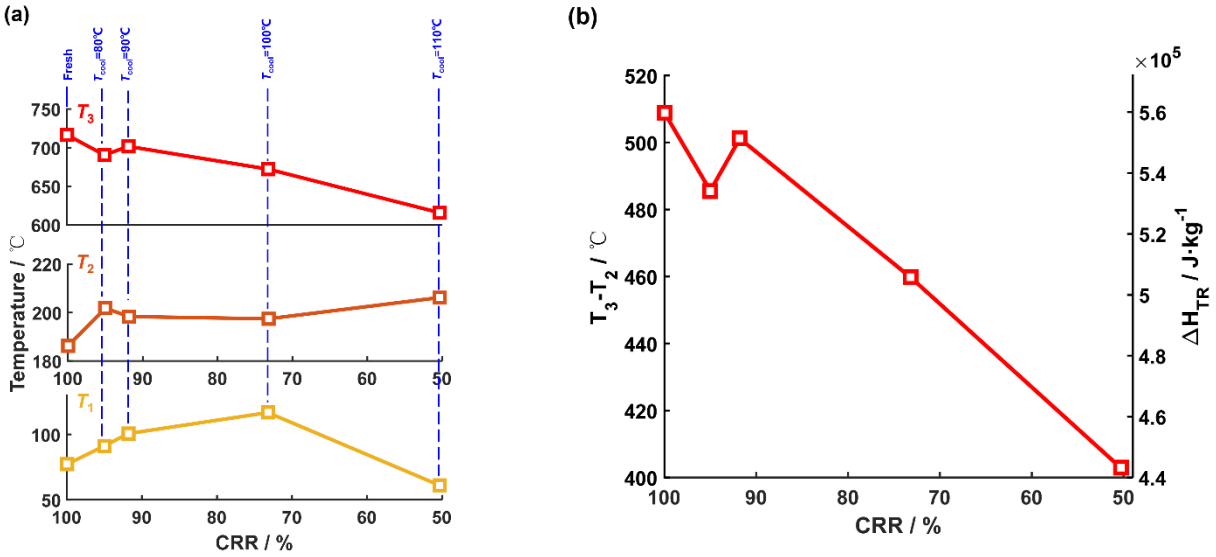

Figure 11. The relationship between the key features of TR and the capacity degradation caused by high-temperature exposure. (a) {T_1, T_2, T_3} vs. CRR. (b) T_3-T_2 and ΔH_{TR} vs. CRR.

4.4 The influence of aging by low-temperature cycling on thermal runaway features

This section discusses the influence of aging by low-temperature cycling on the TR features of lithium-ion batteries. Fig. 12 compares the dT/dt vs. T curves for cell cycled at -10℃ with different CRR. Fig. 12(a) provides an overall view of the dT/dt vs. T curves. The T_3 and the rate of temperature increase after TR are triggered look similar, except for CRR=86.3%, of which the T_3 is much lower. Fig. 12(b) compares the dT/dt vs. T curves for cells cycled to different CRR at low temperature. Obviously the dT/dt increases as the CRR decreases, indicating that a larger amount of lithium deposition leads to poorer thermal stability of the lithium-ion batteries. The poorer thermal stability reflects not only that dT/dt is increasing but also that T_1 is decreasing.

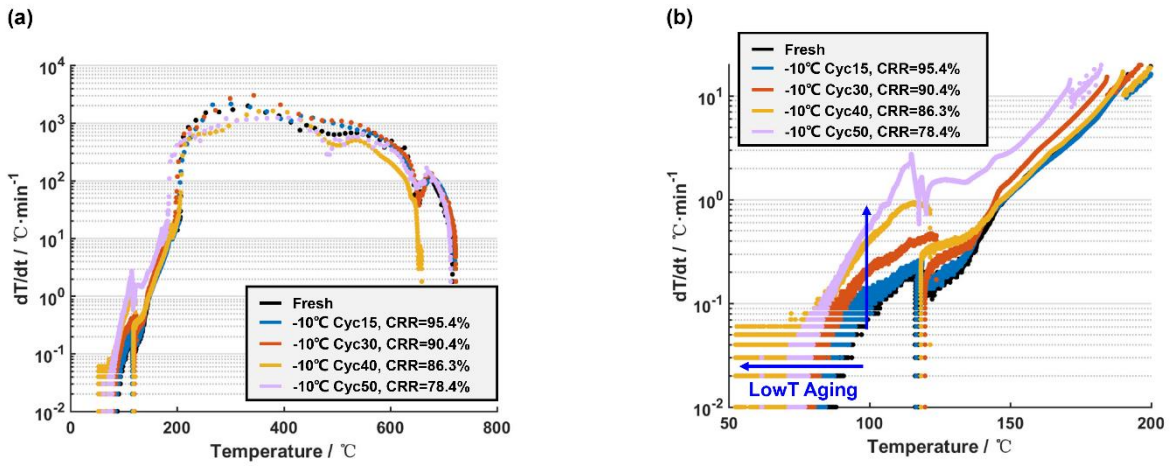

Figure 12. The temperatrue rise rate for fresh cell and aged cells after low-temperature cycling. (a) The overall curve for dT/dt vs. T. (b) The magnified figure of (a) for temperture lower than 200℃.

Fig. 13 presents the key features of TR for cells that are aged by low temperature cycling. Fig. 13(a) displays that as the low-temperature cycle goes on, both T_1 and T_2 drop, whereas T_3 seems to level off. The decreasing trend of T_1 and T_2 means that the thermal stability of the lithium-ion battery becomes worse after low-temperature cycling. The leveling-off trend of T_3 indicates that the total energy that is released during TR will not change after low-temperature cycling, as shown in Fig. 13(b). Therefore the cell after low-temperature cycling will have less thermal stability than the fresh cell, and less than those cells after high-temperature storage. The results here can be inferred to that a cell aged by low-temperature cycling will be more dangerous than itself at fresh condition, similar results can be seen in [28].

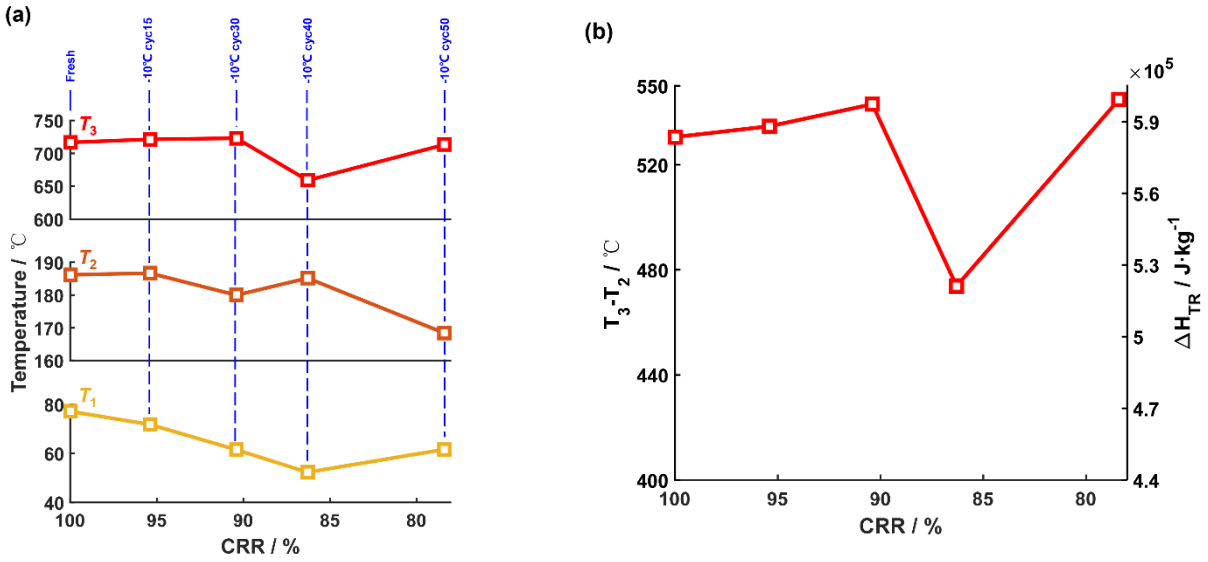

Figure 13. The relationship between the key features of TR and the capacity degradation caused by low-temperature cycling. (a) {T_1, T_2, T_3} vs. CRR. (b) T_3-T_2 and ΔH_{TR} vs. CRR.

4.5 The influence of the aging paths on the thermal runaway features of lithium-ion battery

Although the CRR can be similar for the cells that are exposed to high-temperature and for the cells that are cycled under low temperature, their TR features are quite different, as discussed in Sec. 4.3 and 4.4. This section tries to provide graphical interpretations of the underlying mechanisms.

Fig. 14 presents an interpretation of the mechanisms of the aging effect on the TR features for the cells that are treated by high-temperature exposure. Fig. 14(a) shows the original state of the lithium-ion cell near the interface between the anode and the electrolyte. As the cell has a perfect SEI layer that is formed during manufacturing, it is protecting the further reactions between the electrolyte and the intercalated lithium in the anode. Fig. 14(b) shows that as the temperature increases, the SEI layer decomposes [14], allowing contact between the intercalated lithium and the electrolyte. This process is similar to a reformation of the lithium-ion cells, and the SEI will regenerate, as shown in Fig. 14(c). The regeneration consumes some intercalated lithium, leading to LLI, as found in Sec. 4.1. The decomposition and regeneration process of the SEI compete with each other, and the rate of decomposition will be slower than that of regeneration when the T_{cool} is lower than 110℃. Therefore,

the SEI layer becomes thicker and thicker, as shown in Fig. 14(d), leading to increases in T_1 and T_2. As some of the intercalated lithium has been deactivated in this procedure, T_3 will drop, indicating that there will be less energy released when TR is triggered. If the T_{cool} further increases above 110℃, the rate of SEI regeneration will be faster than that of decomposition, as shown in Fig. 14(e). In this case, the anode loses protection from the SEI layer; therefore, the T_1 will drop, indicating a reduced thermal stability.

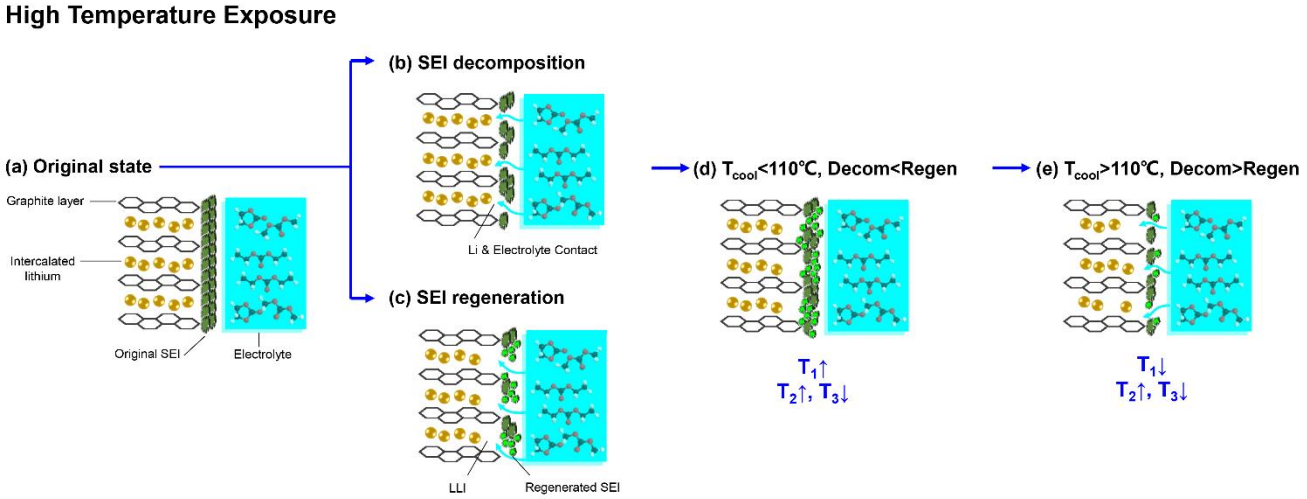

Figure 14. The graphical interpretation of the aging effect on the thermal runaway features for cells after high-temperature exposure.

Fig. 15 illustrates the mechanisms of the aging effect on the TR features for the cells that are treated by low-temperature cycling. Lithium deposition is common for cells cycled under low temperature [41]. The deposited lithium will sit outside the original SEI layer, forming new contact between the lithium and the electrolyte. Therefore the reactivity at the interface of the anode will increase, leading to drops in T_1 and T_2. Moreover, the deposited lithium may grow and pierce the holes of the separator [42], resulting in internal short circuit, which is believed to trigger possible TR in real applications [10, 43].

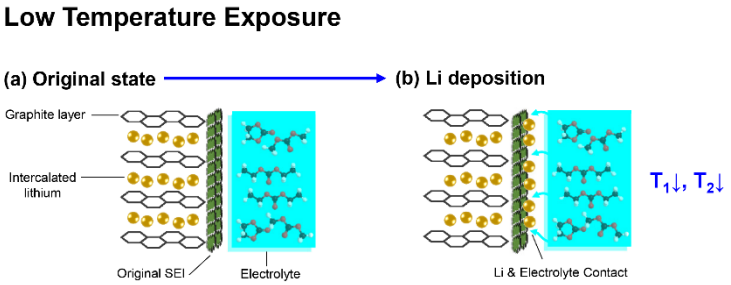

Figure 15. The graphical interpretation of the aging effect on the thermal runaway features for cells after low-temperature cycling.

5. CONCLUSIONS

This paper studies the effects of aging paths on the TR features of lithium-ion batteries using ARC. Characteristic temperatures are defined to quantify the thermal stability of lithium-ion batteries.

The aging effect on change in the characteristic temperatures has been investigated, providing a quantified analysis of the evolution of battery safety during aging. The thermal stability of cells after low-temperature aging is less than that of fresh cells, and less than the cells after high-temperature exposure. Although the CRRs for cells aged by high-temperature exposure and low-temperature cycling can be similar, their thermal stabilities are quite different. The consumption of active lithium at the anode surface to regenerate a new SEI layer will bring a better thermal stability for the cells that are treated by high-temperature exposure. However, if there is lithium deposition on the surface of the anode, the thermal stability of the lithium-ion battery will be reduced. Therefore, when we are investigating the safety of lithium-ion batteries throughout their full life cycle, we must evaluate the changes at the anode surface.

ACKNOWLEDGMENTS
This work is supported by the Ministry of Science and Technology of China (Grant No. 2018YFB0104404 and No. 2016YFE0102200); the National Natural Science Foundation of China (Grant No. 51706117) and (Grant No. U1564205); the China Postdoctoral Science Foundation (Grant No. 2017M610086). The first author thanks the support of "Young Elite Scientist Sponsorship Program" from China Association for Science and Technology.

References

1. X. Chen, W. Lu, C. Chen, M. Xue, *Int. J. Elecrtrochem. Sci.*, 13 (2018) 296.
2. X. Feng, J. Li, L. Lu, J. Hua, L. Xu, M. Ouyang, *J. Power Sources*, 209 (2012) 30.
3. X. Jiang, Z. Yuan, J. Liu, X. Jin, L. Jin, P. Dong, Y. Zhang, Y. Yao, Q. Cheng, C. Liu, Y. Zhang, X. Yu, *Int. J. Electrochem. Sci.*, 13 (2018) 2341.
4. W. Song, F. Bai, M. Chen, S. Lin, Z. Feng, Y. Li, *Appl. Therm. Eng.*, 137 (2018) 203.
5. X. Lai, Y. Zheng, T. Sun, *Elecrochim. Acta*, 259 (2018) 566.
6. Y. Zheng, M. Ouyang, X. Han, L. Lu, J. Li, *J. Power Sources*, 377 (2018) 161.
7. N.E. Galushkin, N.N. Yazvinskaya, D.N. Galushkin. *Int. J. Electrochem. Sci.*, 13 (2018) 1275.
8. M. Chen, F. Bai, W. Song, J. Lv, S. Lin, Z. Feng, Y. Li, Y. Ding, *Appl. Therm. Eng.*, 120 (2017) 506.
9. B. Mao, H. Chen, Z. Cui, T. Wu, Q. Wang, *Int. J. Heat Mass Tran.*, 122 (2018) 1103.
10. X. Feng, X. He, L. Lu, M. Ouyang, *J. Electrochem. Soc.*, 165(2) (2018) A155.
11. X. Lai, Y. Zheng, L. Zhou, W. Gao. *Electrochim. Acta*, 278 (2018) 245.
12. X. Kong, Y. Zheng, M. Ouyang, L. Lu, J. Li, Z. Zhang, *J. Power Sources*, 395 (2018) 358.
13. X. Feng, J. Sun, M. Ouyang, F. Wang, X. He, L. Lu, H. Peng, *J. Power Sources*, 275 (2015) 261.
14. X. Feng, M. Ouyang, X. Liu, L. Lu, Y. Xia, X. He, *Energy Storage Materials*, 10 (2018) 246.
15. T. Wu, H. Chen, Q. Wang, J. Sun, *J. Hazard. Mat.*, 344 (2018) 733.
16. X. Feng, M. Fang, X. He, M. Ouyang, L. Lu, H. Wang, M. Zhang, *J. Power Sources*, 255 (2014) 294.
17. X. Feng, X. He, M. Ouyang, L. Lu, P. Wu, C. Kulp, S. Prasser, *Appl. Energ.*, 154 (2015) 74.
18. X. Feng, L. Lu, M. Ouyang, J. Li, X. He, *Energy*, 115 (2016) 194.
19. W. Song, M. Chen, F. Bai, S. Lin, Y. Chen, Z. Feng, *Appl. Therm. Eng.*, 128 (2018) 1165.
20. C. Weng, X. Feng, J. Sun, H. Peng, *Appl. Energ.*, 180 (2016) 360.
21. X. Feng, J. Li, M. Ouyang, L. Lu, J. Li, X. He, *J. Power Sources*, 232 (2013) 209.
22. S. Wang, L. Shang, Z. Li, H. Deng, Y. Ma, *Int. J. Electrochem. Sci.*, 10 (2015) 5130.
23. Y. Zhu, F. Yan, J. Kang, C. Du, *Int. J. Electrochem. Sci.*, 12 (2017) 6895.
24. J. Yang, Z. Peng, H. Wang, H. Yuan, L. Wu, *Int. J. Electrochem. Sci.*, 13 (2018) 4991.

25. M. Hu, J. Wang, C. Fu, D. Qin, S. Xie, *Int. J. Electrochem. Sci.*, 11 (2016) 577.
26. J. Zhao, Y. Gao, J. Guo, L. Chu, A.F. Burke, *Int. J. Electrochem. Sci.*, 13 (2018) 1773.
27. G. Zhao, F. Xu, *Int. J. Electrochem. Sci.*, 13 (2018) 8543.
28. M. Fleischhammer, T. Waldmann, G. Bisle, B. Hogg, M. Wohlfahrt-Mehrens, *J. Power Sources*, 274 (2015) 432.
29. M. Lammer, A. Königseder, P. Gluschitz, V. Hacker, *J. Electrochem. Sci. Eng.*, 8(1) (2018) 101.
30. J. Zhang, L. Su, Z. Li, Y. Sun, N. Wu, *Batteries*, 2 (2016) 12.
31. M. Ouyang, D. Ren, L. Lu, J. Li, X. Feng, X. Han, G. Liu, *J. Power Sources*, 279 (2015) 626.
32. D. Ren, X. Feng, L. Lu, M. Ouyang, S. Zheng, J. Li, X. He, *J. Power Sources*, 364 (2017) 328.
33. X. Feng, J. Sun, M. Ouyang, X. He, L. Lu, X. Han, M. Fang, H. Peng, *J. Power Sources*, 272 (2014) 457.
34. J. Christensen, J. Newman, *J. Electrochem. Soc.*, 105(11) (2003) A1416.
35. M. Ouyang, X. Feng, X. Han, L. Lu, Z. Li, X. He, *Appl. Energ.*, 165 (2016) 48.
36. D. Yan, L. Lu, Z. Li, X. Feng, M. Ouyang, F. Jiang, *Appl. Energ.*, 179 (2016) 1123.
37. X. Han, M. Ouyang, L. Lu, J. Li, Y. Zheng, Z. Li, *J. Power Sources*, 251 (2014) 38.
38. X. Han, M. Ouyang, L. Lu, J. Li. *J. Power Sources*, 268 (2014) 658.
39. P. Ping, Q. Wang, Y. Chung, and J. Wen. *Appl. Energ.*, 205 (2017) 1327.
40. D. Ren, K. Smith, D. Guo, X. Han, X. Feng, L. Lu, M. Ouyang, J. Li. *J. Electrochem. Soc.*, 165(10) (2018) A2167.
41. M. Ouyang, Z. Chu, L. Lu, J. Li, X. Han, X. Feng, G. Liu, *J. Power Sources*, 286 (2015) 309.
42. A. Jana, D.R. Ely, R.D. García. *J. Power Sources*, 275 (2015) 912.
43. X. Feng, C. Weng, M. Ouyang, J. Sun. *Appl. Energ.*, 161 (2016) 168.